

## Article

# Modelling Deaggregation Due to Normal Carrier–Wall Collision in Dry Powder Inhalers

Francesca Orsola Alfano <sup>1,\*</sup> , Alberto Di Renzo <sup>1,\*</sup> , Roberto Gaspari <sup>2</sup>, Andrea Benassi <sup>2,3</sup>  
and Francesco Paolo Di Maio <sup>1</sup> 

<sup>1</sup> DIMES Department, University of Calabria, 87036 Rende, Italy

<sup>2</sup> Chiesi Farmaceutici SpA, 43122 Parma, Italy

<sup>3</sup> International School for Advanced Studies (SISSA), 34136 Trieste, Italy

\* Correspondence: francesca.alfano@unical.it (F.O.A.); alberto.direnzo@unical.it (A.D.R.)

**Abstract:** Powder deaggregation in Dry Powder Inhalers (DPI) with carrier-based formulations is a key process for the effectiveness of drug administration. Carrier-wall collisions are one of the recognised mechanisms responsible for active pharmaceutical ingredient (API) aerosolisation, and DPI geometries are designed to maximise their efficacy. The detachment of fine and cohesive API particles is investigated at a fundamental level by simulating with DEM the normal collision of a carrier sphere with an API particle attached. The impact velocity at which detachment occurs (escape velocity) is determined as a function of key parameters, such as cohesiveness, coefficient of restitution, static and rolling friction. An analytical model for the escape velocity is then derived, examining the role of the initial position of the particle, cohesion model and particle size. Finally, the results are framed in the context of DPI inhalers, comparing the results obtained with impact velocities typically recorded in commercial devices.

**Keywords:** dry powder inhalers; DEM simulations; carrier-based formulations; deaggregation



**Citation:** Alfano, F.O.; Di Renzo, A.; Gaspari, R.; Benassi, A.; Di Maio, F.P. Modelling Deaggregation Due to Normal Carrier–Wall Collision in Dry Powder Inhalers. *Processes* **2022**, *10*, 1661. <https://doi.org/10.3390/pr10081661>

Received: 13 July 2022

Accepted: 15 August 2022

Published: 21 August 2022

**Publisher's Note:** MDPI stays neutral with regard to jurisdictional claims in published maps and institutional affiliations.



**Copyright:** © 2022 by the authors. Licensee MDPI, Basel, Switzerland. This article is an open access article distributed under the terms and conditions of the Creative Commons Attribution (CC BY) license (<https://creativecommons.org/licenses/by/4.0/>).

## 1. Introduction

Dry Powder Inhalers (DPI) are medical devices used to deliver powder medication into the lungs. They are commonly applied for the treatment of respiratory diseases, such as asthma and chronic obstructive pulmonary disease (COPD), but several other solutions are under development, e.g., for antituberculosis and anticancer drugs, antibiotics [1] and vaccines, including SARS-CoV-2 [2].

The medication dose can be made available in blisters, capsules or directly exposed to the air flow. To overcome issues associated with the flowability of the fine and cohesive powders, they are manufactured in a carrier-based formulation, in which the Active Pharmaceutical Ingredient (API) is adhered to coarser carrier particles (50–200  $\mu\text{m}$ ) to form “ordered mixtures”. The API needs to be in the range of 1–10  $\mu\text{m}$  to be respirable and reach the lower lung airways [3]; such small particles are subjected to van der Waals and electrostatic forces [4–6], which cause adhesion phenomena and reduced flowability [7,8]. The use of carrier particles thus improves manufacturability and flow properties. The DPI is then designed to promote the dose aerodispersion and the subsequent “aerosolization”, i.e., detachment of the API during inhalation. Microscopically, the delivery process is governed by the local interaction between the air flow dynamics caused by the patient’s inhalation and the solids’ geometrical, physical and surface properties [9].

One of the main mechanisms of powder deaggregation is the impact of carrier particles with the wall. To gain a deeper understanding of the extent of such phenomena, experimental work has been carried out via image analysis techniques. Particle Image Velocimetry (PIV) has been used to obtain instantaneous velocity measurements of the fluid flow in

DPI [10–12]. High-speed photography measurements have been applied to study carrier motion [11,13] and API–carrier detachment phenomena [14] in specially designed transparent DPI.

DEM simulations can be a useful tool to obtain detailed information and insights into the deaggregation process of different drug formulations [15]. DEM simulations have been carried out to study API deaggregation due to carrier–wall impact [16] and carrier–carrier impact [17]. The effect of carrier surface roughness on deaggregation was also investigated [18]. Tong et al. [19] evaluated the collision energy occurring in DPI devices and found that the particle–wall collision plays a dominant role in powder deaggregation. The detachment of fine adhered dust particles during bulk particle contacts has been recently studied by Schulz et al. [20], using both the DEM approach with JKR cohesion model and dust detachment functions.

By introducing the effect of the fluid phase through the CFD-DEM approach, Yang et al. [21] analysed the detachment of API particles due to aerodynamic forces. More recently, fully coupled CFD-DEM simulations have been applied to study realistic API–carrier blends in the entire inhaler [22–24]. Although recognised as a key factor for aerosolisation [25], the effectiveness of the collisions in relation to breaking the cohesive bond between API and carrier particles and determining deaggregation is not yet fully understood and predictable. For example, API rotational motion before detachment is not considered in previous models. In addition, different cohesion models have been used for inter-particle adhesion, making it hard to compare the results.

In the present work, the carrier–wall collision detachment mechanism is analysed at a fundamental level, by considering DEM simulations of a single carrier particle with an adhered API particle subjected to wall collisions under various conditions. The detachment dynamics by normal impact with a wall are analysed in detail, and the importance of models and parameter tuning are discussed. To generalise the results in terms of predictive power, starting from three cohesive models' formulations, a general analytical model to estimate the escape velocity, and the detachment conditions are developed and validated.

## 2. Materials and Methods

The detachment of API fine and cohesive particles from coarse carrier particles due to carrier–wall collisions was investigated using DEM simulations.

The open source software used for the simulations was MFIX [26].

### DEM Approach

In the DEM approach, particles are individually tracked along their deterministic motion in the device, as resulting from the calculation of all forces acting on them.

The position ( $\vec{x}_i$ ) and linear ( $\vec{v}_i$ ) and angular ( $\vec{\omega}_i$ ) velocities of the  $i$ th particle evolve according to Newton's second law of motion:

$$\frac{d\vec{x}_i}{dt} = \vec{v}_i \quad (1)$$

$$m_i \frac{d\vec{v}_i}{dt} = \vec{F}_T = \sum_{j=i}^{N_c} \vec{F}_{c,ij} + \vec{F}_{coh,ij} + \vec{F}_{d,i} + \vec{F}_{b,i} + \vec{F}_{l,i} + \vec{F}_{g,i} \quad (2)$$

$$I_i \frac{d\vec{\omega}_i}{dt} = \vec{T}_T = \sum_{j=i}^{N_c} \vec{T}_{c,ij} + \vec{T}_r \quad (3)$$

where  $\vec{F}_T$  is the net sum of all the forces acting on the  $i$ th particle: contact (subscript  $c$ ), cohesion (subscript  $coh$ ), drag (subscript  $d$ ), pressure gradient (subscript  $b$ ), lift (subscript  $l$ ) and gravitational (subscript  $g$ ) forces;  $\vec{T}_T$  is the sum of all torques acting on the  $i$ th particle: contact torque ( $\vec{T}_c$ ) and rolling resistance ( $\vec{T}_r$ ).

The simulation of API–carrier complexes requires careful consideration of the interaction between the elastic-dissipative contact forces and the cohesive interactions. The contact forces are calculated according to the Hertz–Mindlin no-slip model [27].

The normal ( $F_{c,ij}^{(n)}$ ) and tangential ( $F_{c,ij}^{(t)}$ ) contact forces are calculated as follows:

$$F_{c,ij}^{(n)} = -\frac{4}{3}E_{eq}\sqrt{R_{eq}}\delta_n^{\frac{3}{2}} - \eta_n^H \delta_n^{\frac{1}{4}}v_n \quad (4)$$

$$F_{c,ij}^{(t)} = \min(-\mu_s F_{c,ij}^{(n)}, -8G_{eq}\sqrt{R_{eq}}\delta_n^{\frac{1}{2}}\delta_t - \eta_t^H \delta_n^{\frac{1}{4}}v_t) \quad (5)$$

where  $\delta$  represents the (normal and tangential) displacement between the contacting particles,  $v$  their relative velocity at the contact point,  $\eta^H$  the damping coefficients and  $\mu_s$  the static friction coefficient.  $R_{eq}$ ,  $E_{eq}$  and  $G_{eq}$  are the equivalent properties (radius, Young modulus and shear modulus) of the contact between particles  $i$  and  $j$  (see, e.g., Di Renzo and Di Maio [28]).

Cohesive models consider attractive forces in the normal direction, so the tangential motion of API particles would be unrestricted provided there is no tangential displacement, for example, in the case of pure rolling, with the possible consequence of endless rolling of attached particles. To prevent such condition, a rolling resistance torque or rolling friction opposing the rotation of particles is added in Equation (3). This term is calculated according to the Constant Directional Torque model (CDT, Ai et al. [29]):

$$\vec{T}_r = -\mu_r R_{eq} |F_{c,ij}^{(n)}| \frac{\vec{\omega}_i - \vec{\omega}_j}{|\vec{\omega}_i - \vec{\omega}_j|} \quad (6)$$

in which  $\mu_r$  is the user-defined rolling friction coefficient,  $F_{c,ij}^{(n)}$  is the normal contact force between objects  $i$  and  $j$ ,  $\omega_i$  and  $\omega_j$  are the angular velocities of objects  $i$  and  $j$ , and  $R_{eq}$  is the equivalent radius.

### Cohesion Models

As anticipated, pharmaceutical powders are nearly always particles with poor flowability properties. To account for the API–carrier interactions, different models have been considered in simulations, the most common of which are denoted by the following acronyms: JKR, SJKR, VDW. Their force–displacement relationships for typical conditions are illustrated in the Figure, and the corresponding formulas are summarized in the following subsections.

**Johnson–Kendall–Roberts (JKR).** An accurate description of the contact between cohesive–adhesive bodies can be obtained with the well known Johnson–Kendall–Roberts (JKR) contact model [30]. The basis of the JKR model is the hypothesis that adhesive-type interactions occur between the “flattened” region of the surfaces of the colliding particles, i.e., the deformed contact region.

The normal contact force is a function of the normal overlap,  $\delta_n$ , and the cohesion surface energy,  $\gamma$ , in which the two components (elastic and cohesive) are linked and cannot be separated:

$$F_{el,JKR} = 4\sqrt{\pi\gamma E_{eq}}a^{3/2} - \frac{4E_{eq}}{3R_{eq}}a^3 \quad (7)$$

$$\delta_n = \frac{a^2}{R_{eq}} - \sqrt{\frac{4\pi\gamma a}{E_{eq}}} \quad (8)$$

where  $a$  is the radius of the contact area,  $E_{eq}$  is the equivalent Young modulus.

According to the JKR contact model, the cohesive interaction acts also at “negative overlaps” during the detachment phase, i.e., when the two objects, considered as undeformed spheres, would no longer be in contact. This is due to the deformation caused by the cohesive force during the contact, which holds the surfaces together and forms a neck, with the consequence that contact persists up to a maximum of attractive force called

pull-off force. In order for the particles to detach, the force that separates them must exceed this force and the nominal distance between the particles (between the spheres considered undeformed) must exceed the maximum distance, a condition at which a jump in the resisting force is observed and the particles become suddenly separated.

Simplified JKR (SJKR). A considerably simplified model, known as a linear cohesion model and referred to as SJKR, is available in some DEM software, such as LIGGGHTS [31]. Cohesion and adhesion phenomena are modeled through the insertion of an additional force,  $F_{coh}$ , which is directly proportional to the contact area between the two contacting bodies,  $A_{cont}$ :

$$F_{coh} = kA_{cont} \quad (9)$$

where  $k$  is the cohesion energy density (dimensionally: N/m<sup>2</sup>) and  $A_{cont}$  is the geometric contact area between the two particles, which can be calculated according to Hertz contact theory from the following:

$$A_{cont} = \pi R_{eq} \delta_n \quad (10)$$

where  $R_{eq}$  is the equivalent radius and  $\delta_n$  is the normal overlap. This formulation is used in the software EDEM [32].

The cohesive force acts only when  $A_{cont} > 0$  and, therefore, when the two bodies are in contact; in the case of two spheres, when the distance between their centers is less than the sum of the radii.

The force calculated by Equation (9) is added to the Hertzian normal elastic contact force, as they act in opposite directions. The total elastic force acting in normal direction is thus given by:

$$F_{el,sjkr} = kA_{cont} - \frac{4}{3} E_{eq} \sqrt{R_{eq} \delta_n^3} \quad (11)$$

Van der Waals/constant surface energy (VDW). The VDW model is the cohesion model available by default in the MFIX software [33]. The cohesive/adhesive forces are accounted for using a combination of a van der Waals interaction between distant particles and constant surface energy model for particles in contact:

$$F_{coh} = \begin{cases} 0 & z > z_{out} \\ \frac{A \cdot 2R_{eq}}{12z^2} & z_{in} < z \leq z_{out} \\ 2\pi\gamma(2R_{eq}) & z \leq z_{in} \end{cases} \quad (12)$$

where  $z$  is the distance between the surfaces of the two particles involved,  $R_{eq}$  is the equivalent radius,  $A$  is the Hamaker constant,  $z_{in}$  and  $z_{out}$  are the inner and outer cutoff, respectively, and  $\gamma$  is the surface energy.

Both the SJKR and JKR models have been implemented in the in-house version of the code MFIX.

### 3. DEM Model of the Detachment Process

#### 3.1. Simulation Set-Up and Parameters

To investigate the full dynamics of the carrier-API particle collision with a wall, DEM simulations are carried out for a simple geometry in which a carrier particle with one API particle stuck on its side impacts normally against a flat wall. The setup of the simulation is shown in Figure 1, where the carrier particle is in grey and the smaller API particle is in pink. Taking the wall normal as axis for the carrier, the fine particle is said to be located at the equatorial position. The API particle's overlap is set to the equilibrium value between elastic repulsive and adhesive forces, and both particles are assigned the same instantaneous velocity normal to the wall. Note that the possibility of vibration-induced detachment is not directly contemplated, as it would require contact models currently unavailable in the literature, to the best of the authors knowledge. Finally, for the range of cohesive forces involved, the negligible action of gravity is not considered. The physical and mechanical properties are reported in Table 1. They have been selected in order to

reproduce the behavior of brittle, irregularly shaped pharmaceutical particles, such as lactose (see e.g., Alfano et al. [22]).

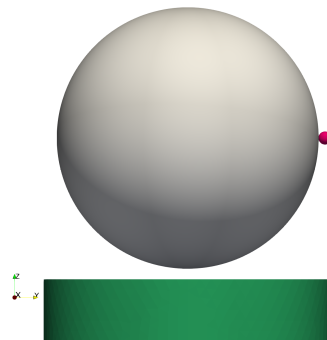


**Figure 1.** System with two particles and a wall used in the simulations.

**Table 1.** Physical and mechanical properties used in the simulations (PP = particle–particle; PW = particle–wall).

|                                   | API            | Carrier        | Wall |
|-----------------------------------|----------------|----------------|------|
| $R$ ( $\mu\text{m}$ )             | 5              | 100            | -    |
| $\rho$ ( $\text{kg}/\text{m}^3$ ) | 1500           | 1500           | -    |
| $E$ (MPa)                         | 5              | 5              | 5    |
| $\nu$ (-)                         | 0.20           | 0.20           | 0.20 |
| $e$ (PP and PW) (-)               | 1 (PP), 1 (PW) | 1 (PP), 1 (PW) | -    |
| $\mu_s$ (-)                       | 0.45           | 0.45           | 0.45 |
| $\mu_r$ (-)                       | 0.30           | 0.30           | 0.30 |

Depending on the conditions examined, the API particle will either remain stuck along the carrier surface or it will detach. If the impact dynamical effects overcome the action of adhesion, the API particle will detach at some point; otherwise, the particle will remain attached on the surface, although this does not necessarily imply it will remain static, as discussed below. In some of the simulations, the CDT rolling friction model (Equation (6)) is activated. The timestep used in the simulations is  $6 \times 10^{-7}$  s.

The static friction and restitution coefficients are varied. Purely elastic (coefficient of restitution  $e = 1$ ) impacts are considered initially, and the effect of varying this parameter is investigated later.

The cohesion model used in the simulations is SJKR. As anticipated earlier, the cohesive force is directly proportional to the contact area through the cohesion energy density,  $k$ . The selection of the value for the energy density is based on the conditions of force and overlap at the equilibrium between the adhesive force and the elastic repulsion, starting from a reference value of the force set by the dimensionless granular Bond number, ( $B_0 = \text{adhesive-cohesive force } (F_E)/\text{weight } (F_g)$  of the lightest particle [34,35]).

The cohesion energy density is obtained as:

$$k = \frac{F_E}{A_{cont}} \quad (13)$$

in which the equilibrium force is calculated by assigning a characteristic Bond number,

$$F_E = B_0 \cdot F_{g,API} \quad (14)$$

and the contact area is calculated according to Equation (10), where the equilibrium overlap is derived from the Hertz contact model:

$$\delta_E = \sqrt[3]{\frac{1}{R_{eq}} \left( \frac{3 F_E}{4 E_{eq}} \right)^2} \quad (15)$$

In the current study, different levels of cohesion will be examined by setting different values of the granular Bond number, as reported in Table 2, together with the corresponding equilibrium overlaps and cohesion energy density. The Bond value  $Bo = 33,520$  is calculated from the pull-off force between glass beads and salbutamol sulphate powder measured experimentally via AFM by Cui et al. [36].

The value of  $k$  as a function of the Bond number (calculated according to Equation (13)) is reported in Figure 2, for values of  $Bo$  ranging from 0 to 60,000.

**Table 2.** Equilibrium overlap and cohesion energy density for different values of the Bond number.

| <b>Bo</b> | <b><math>\delta_E</math> (nm)</b> | <b><math>k</math> (J/m<sup>3</sup>)</b> |
|-----------|-----------------------------------|-----------------------------------------|
| 500       | 6                                 | 40,420                                  |
| 5000      | 30                                | 87,090                                  |
| 33,520    | 105                               | 164,200                                 |
| 50,000    | 137                               | 187,500                                 |

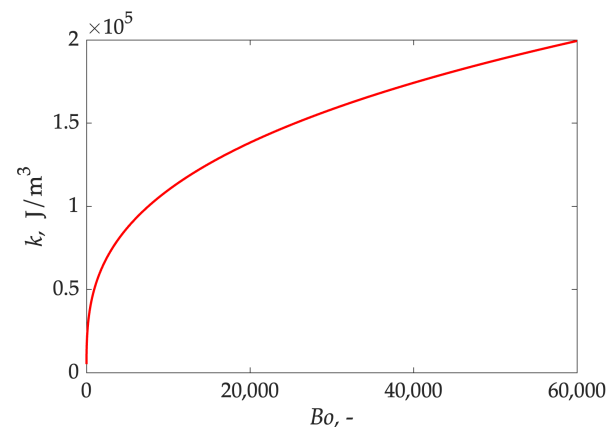


**Figure 2.** Relationship between the cohesion energy density and the Bond number.

### 3.2. Escape Velocity

After the carrier hits the wall, the relative velocity between the two contacting particles changes abruptly. Two possible scenarios follow: if the kinetic energy of the impact overcomes the work of adhesion, the API particle escapes; otherwise, the API particles remains on the carrier. The minimum velocity determining detachment is referred to as *escape velocity*,  $v_e$  [16].

The determination of the escape velocity is carried out by a sequence of DEM simulations with different levels of cohesion and activating or deactivating the rolling friction model. For each value of  $Bo$  considered (see Table 2), the interval containing the escape velocity is found between “low” initial velocity, at which the API particle remains stuck, and “high” velocity, where the API particle escapes. The interval is then progressively narrowed following the bisection method on the initial velocity. The results, reported in Table 3, are accurate to the second decimal place (in m/s).

**Table 3.** Escape velocity as a function of Bond number with (RF) and without (no RF) rolling friction.

| <b>Bond Number, <math>Bo</math></b> | <b>Escape Velocity, (m/s), RF</b> | <b>Escape Velocity, (m/s), No RF</b> |
|-------------------------------------|-----------------------------------|--------------------------------------|
| 500                                 | 0.15                              | 0.15                                 |
| 5000                                | 0.57                              | 0.54                                 |
| 33,520                              | 1.81                              | -                                    |
| 50,000                              | 2.33                              | 1.77                                 |

### 3.3. Influence of Dissipation Parameters

Beyond the effect of the intensity of the cohesion, other parameters influencing the dynamics of the contact are the restitution coefficient, responsible for the velocity-dependent

dissipation in the normal (and tangential direction) and the friction coefficient, determining dissipation due to a sliding contact.

Figure 3 shows the escape velocity as a function the restitution coefficient,  $e$ , for three values of the static friction coefficient,  $\mu_s$ . The same values are applied to both PW and PP contact. Note that whenever a parameter is changed, all values for the different contacts (all combinations of particle–particle and particle–wall) are changed simultaneously. In addition, the tangential restitution coefficient is changed alongside the normal restitution coefficient. The results show that both parameters have an effect on the velocity at which the detachment occurs.

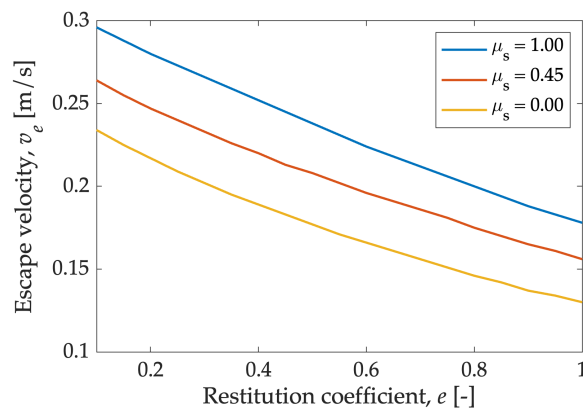


**Figure 3.** Escape velocity as a function of coefficient of restitution ( $e$ ) and static friction coefficient ( $\mu_s$ ). Level of cohesion:  $B_0 = 500$  with cohesion model SJKR. Rolling friction is active.

The restitution coefficient translates into the velocity-dependent dissipation force that acts against the relative velocity at contact. In the case of the API detaching from the carrier, the most important effect manifests in the normal direction as the API particle is pushed by the inertia out of the carrier surface. As the API particle starts in contact, the resisting dissipative force counteracts the detachment process, as the relative velocity will be directed toward detaching. Therefore, it is reasonable to expect that as the restitution coefficient decreases, and the damping coefficient  $\eta_n^H$  increases, the detachment process becomes harder and the escape velocity increases.

The friction coefficient  $\mu_s$  limits the maximum tangential force that the contacting surfaces can exert on the API particle as soon as the carrier particle impacts and rebounds on the wall. So, as the friction coefficient increases, the API particle can be subjected to a higher resisting force at the contact. Obviously, after the first few instants, the local conditions will evolve with the API particle that translates and rotates to some extent on the carrier surface before detaching. However, this initial role played by the tangential force is likely to explain why the curves in Figure 3 for the escape velocity at higher friction coefficient values are above those at lower values.

The results obtained are also useful for understanding what happens to real powders. For example, powders that tend to deform elastically will have a lower release rate than materials that dissipate during impact, while materials with a high coefficient of static friction will detach with greater difficulty.

### 3.4. The Role of Rolling Friction

The results reported in Table 3 proved that the use of a rolling friction model in the DEM simulation has an influence in the detachment mechanism of the API particles. With the aim of understanding with greater detail what happens during the carrier–wall collision, four DEM simulations were carried out to closely follow the velocity changes during impact by using a smaller integration step (60 ns) and storing the results at each timestep. The reference Bond order is 33,520.

In the first two simulations, the initial carrier velocity is 2.0 m/s; one is without rolling friction, the other with rolling friction. In the other two simulations, at lower initial carrier velocity, 1.0 m/s and 1.8 m/s, the first one is without rolling friction and the second one with it.

The results, in terms of vertical component of velocity profile during collision, are reported in Figure 4, along with snapshots of the position of particles at the end of the simulation.

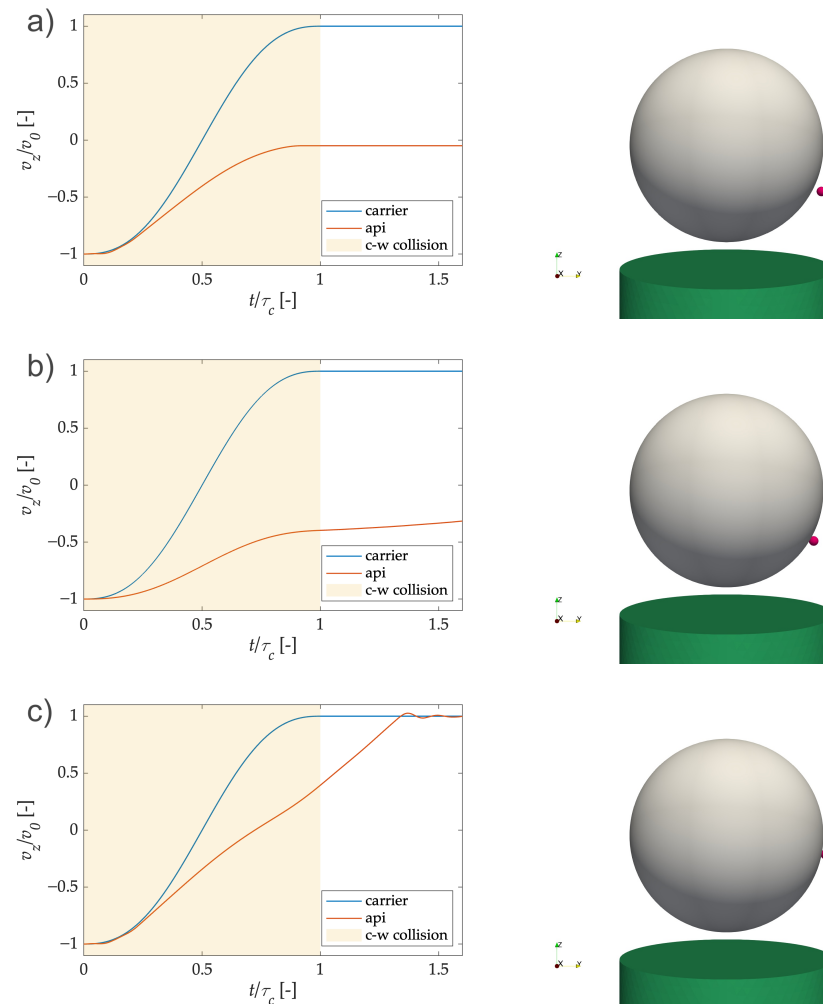


**Figure 4.** Carrier and API dimensionless velocity profiles during wall collision and particle position after impact (at  $t = 1.6\tau_c$ ) in three cases: (a) detachment of API particle, (b) no detachment of API particle without rolling friction, (c) no detachment of API particle with rolling friction. The shaded area indicates carrier contact with the wall.

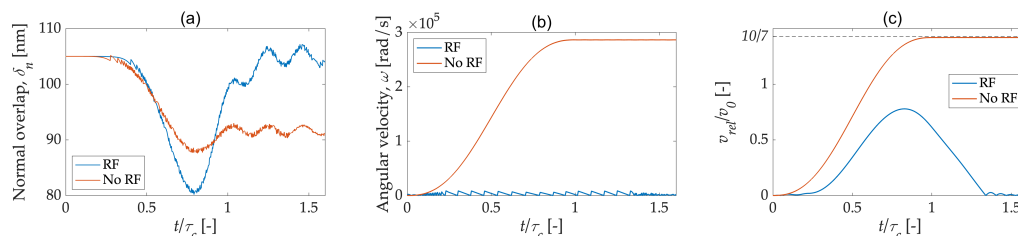
To directly compare the different scenarios, the time and velocity variables are normalized, by the collision duration and the initial velocity of the carrier, respectively. The shaded area in the plot indicates the carrier particle contact with the wall.

Figure 4a shows the velocity profiles obtained when detachment occurs. The velocity of the carrier particle, initially directed downwards, starts decreasing (in magnitude) until it reaches zero. At the point of rebound, since the collision is elastic, the carrier particle will return to its initial velocity, directed upwards. After detachment, the API particle continues its motion downwards with a lower velocity (in magnitude), as a result of the energy dissipated during detachment. Analogous plots are obtained whether rolling friction is activated or not, but the velocity at which the detachment occurs is different.

If rolling friction is not activated and the particle does not detach (Figure 4b), the API particle will start rolling on the carrier surface. If rolling friction is activated, the API starts

the rolling movement but stops after a few timesteps, by remaining in a fixed position when the carrier rebounds. As shown in Figure 4c, the velocity of the API will eventually reach the velocity of the carrier.

A comparison between the two cases with API detachment, in the presence and absence of rolling friction (RF), is reported in Figure 5.



**Figure 5.** Evolution of (a) overlap, (b) angular velocity and (c) relative velocity of the API particle (with respect to the carrier) during detachment with and without rolling friction (RF).

Figure 5a shows the normal overlap between API and carrier in the two simulations. In both cases, the two particles start from the equilibrium overlap, 105 nm. During the first part of carrier–wall collision, the overlap starts decreasing. At the end of the collision, the overlap will oscillate around the initial value if rolling friction is active, while it will settle to a lower value if rolling friction is not active, and therefore the API will roll on the carrier surface.

Figure 5b shows the angular velocity of the API particle as a function of time for the two cases considered. If RF is activated, the angular velocity oscillates throughout the simulation, with an average value that is around 4000 rad/s. If there is no rolling friction, the angular velocity increases during the impact, reaching almost 300,000 rad/s. The API will then continue to orbit on the carrier with constant angular velocity following a uniform circular motion.

Figure 5c shows the relative velocity (magnitude) between the API and the carrier, normalized with the initial value of the carrier velocity (1 m/s without RF, 1.81 m/s with RF). Initially, the API moves with the carrier, so its relative velocity is zero. As previously noted, if the rolling friction is active, the velocity of the API initially deviates from that of the carrier, and then returns to its initial value. If, on the other hand, the rolling friction is not active, the trend of the relative velocity is the same as that of the angular velocity, with a progressive increase until it reaches 10/7 of the initial value. The increase in relative velocity is in fact closely related to the increase in angular velocity. The final value of the relative velocity of the API is 10/7 · 1 m/s, about 1.43 m/s. By dividing this value by the radius of the carrier particle, 5  $\mu$ m, the exact final value of the angular velocity is obtained,  $\sim 286,000$  rad/s.

#### 4. Analytical Model for the Escape Velocity

As shown by the analysis in the previous Section, the determination of the escape velocity by means of a set of DEM simulations can be time-consuming. So, for example repeating the exercise for an initial position of the API particle different than the equator as a function of the particle properties and model parameters would easily become problematic. An alternative, general analytical model to directly estimate the escape velocity as a function of the properties of the materials and the position of the API particle is presented in this section.

A carrier particle on which an API particle adheres with initial equilibrium overlap,  $\delta_0$  and initial velocity  $v_0$  is considered. The effects of gravity and the surrounding air are neglected. The restitution coefficient is assumed to be unity. As it will be shown below, the treatment can be applied to any initial position of the API particle on the carrier surface. The presentation will start by the two “south Pole” and “equator” positions of the API, and then the results will be generalized to any starting position in the hemisphere.

#### 4.1. South Pole Detachment

The first considered case is illustrated in Figure 6a. The instantaneous initial velocity of the API particle is directed along the direction joining the two centers of the particles. The API particle is impulsively subjected to a velocity  $v_0$ , while the carrier particle is assumed to remain static, in analogy to the case where a wall blocks its position.

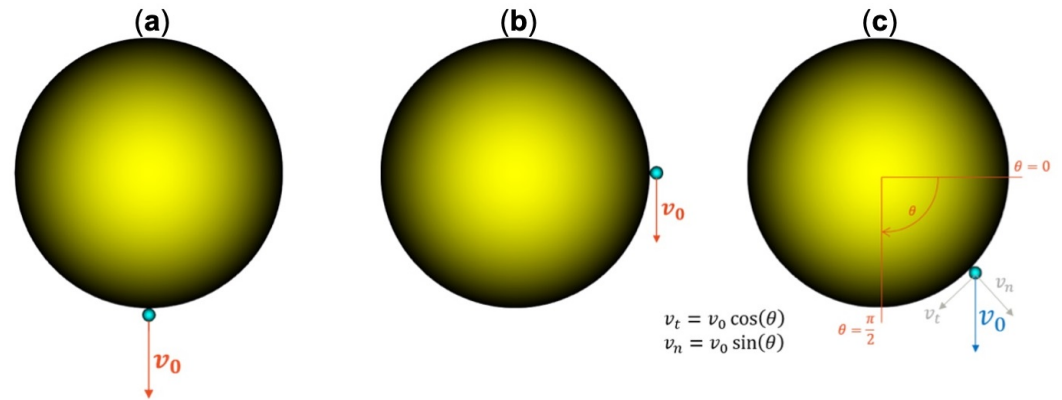


**Figure 6.** (a) API particle in south pole position, (b) API particle in equatorial position, (c) API particle attached in a generic position in the south hemisphere.

Instead of resorting to the dynamic evolution of the contact forces and displacements, a simpler and more elegant description of the API detachment process is carried out in terms of the associated energy. In the absence of gravity, the API particle detaches if its initial kinetic energy,  $E_k$ , overcomes the energy associated to cohesive interaction at the contact:

$$E_k = \frac{1}{2} m_{API} v_0^2 \geq E_{coh} \quad (16)$$

in which  $m_{API}$  is the mass of the API particle and  $E_{coh}$  has to be calculated for the specific cohesion model.

By equating the two energy terms in Equation (A50) the escape velocity is directly calculated:

$$v_{e,sp} = \sqrt{\frac{E_{coh}}{\frac{1}{2} m_{API}}} \quad (17)$$

#### 4.2. Equatorial Detachment

In this second case, shown in Figure 6b, the API particle is in the equatorial position with respect to the carrier. The force that keeps the API on the carrier acts in the horizontal direction, while the velocity  $v_0$  is directed vertically. In order to compare the two competing actions, it is necessary to consider that the action of adhesion is as a centripetal force, while the action of the initial, tangential velocity is centrifugal.

If the initial velocity  $v_0$  is insufficient to determine detachment, the particle begins to rotate around the carrier, as shown in the DEM simulations presented earlier: part of the translational kinetic energy is converted into rotational energy (with the API particle acquiring a certain angular velocity  $\omega_f$ ); after an initial transfer of translational to rotational kinetic energy, the final translational velocity of the particle ( $v_f$ ) is equal to 5/7 of the initial velocity  $v_0$ . A detailed derivation of this universal result is discussed in Appendix A.

If, on the other hand, the inertial effect of initial velocity  $v_0$  is high enough to overcome the cohesive centripetal force, the API particle will achieve detachment. A centrifugal force acting in tangential direction can be associated to  $v_0$ :

$$F_{fc} = \frac{m_{API}}{R_C + R_{API}} v_0^2 \quad (18)$$

in which  $R_C$  and  $R_{API}$  are the radii of the carrier particle and of the API particle, respectively. To detach the API from the carrier, this force must carry out a work  $L_{fc}$  such as to bring the initial overlap between the two particles ( $\delta_0$ ) to the the minimum overlap (zero or negative, depending on the cohesion model), overcoming the cohesion energy:

$$L_{fc} = \int_0^{\delta_0} F_{fc} d\delta = \frac{m_{API}}{R_C + R_{API}} v_0^2 \delta_0 \geq E_{coh} \quad (19)$$

The critical escape velocity,  $v_{e,eq}$ , is then obtained by:

$$v_{e,eq} = \sqrt{\frac{E_{coh}}{\frac{m_{API}}{R_C + R_{API}} \delta_0}} \quad (20)$$

#### 4.3. General South-Hemisphere Detachment

The two cases presented so far can be combined to generalise the treatment in the case in which the API is positioned at a generic angle on the lower (“South”) hemispherical carrier surface by introducing the angle variable  $\theta$ , as shown in Figure 6c. An angle of 0 degrees corresponds to equatorial position and 90 degrees to the South pole. The velocity  $v_0$  can be decomposed into the two normal and tangential components,  $v_n$  and  $v_\theta$ , respectively.

The  $v_n$  component comes into play in the kinetic energy, while  $v_\theta$  in the work associated with the centrifugal force. Detachment occurs if:

$$L_{fc} + E_k \geq E_{coh} \quad (21)$$

with:

$$E_k = \frac{1}{2} m_{API} v_n^2 = \frac{1}{2} m_{API} v_0^2 \sin^2 \theta \quad (22)$$

and:

$$L_{fc} = \frac{m_{API}}{R_C + R_{API}} v_\theta^2 \delta_0 = \frac{m_{API}}{R_C + R_{API}} \cos^2 \theta v_0^2 \delta_0 \quad (23)$$

The escape velocity, or the critical detachment value, is given by:

$$v_e = \sqrt{\frac{E_{coh}}{m_{API} \left( \frac{\delta_0 \cos^2 \theta}{R_C + R_{API}} + \frac{1}{2} \sin^2 \theta \right)}} \quad (24)$$

By making explicit use of the previous results, if the values of critical escape velocities from the equator ( $v_{e,eq}$ , Equation (A49)) and south pole ( $v_{e,sp}$ , Equation (A51)) are known, the escape velocity can also be expressed as:

$$v_e = \sqrt{\frac{1}{\frac{1}{v_{e,eq}^2} \cos^2 \theta + \frac{1}{v_{e,sp}^2} \sin^2 \theta}} \quad (25)$$

#### 4.4. Calculation of Cohesion Energy

The energy associated to cohesion, indicated as  $E_{coh}$ , depends on the cohesion model. In the present work, the three cohesion models already described are analysed: SJKR, VDW and JKR. Assuming that at the beginning the API particle is placed on the carrier particle with an overlap equal to that of equilibrium  $\delta_E$ , the cohesion energy for the three models can be represented by the coloured areas in Figure 7 and corresponds to the work necessary to break the API-carrier contact. The curves shown have been obtained starting from the parameters used in later calculations (see Table 4 for the parameters).

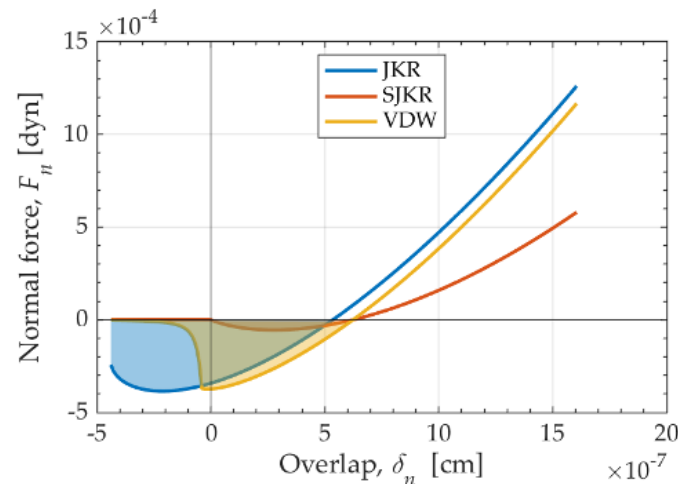


**Figure 7.** Illustration of the cohesion energy with the three cohesion models VDW, JKR, SJKR.

The cohesion energy with the SJKR model is given by:

$$E_{coh} = \frac{k\pi R_{eq}}{2} \delta_E^2 - \frac{8}{15} E_{eq} \sqrt{R_{eq}} \delta_E^{2.5} \quad (26)$$

while the cohesion energy with the VDW model is:

$$E_{coh} = A \frac{R_{eq}}{6} \left( \frac{1}{z_{in}} - \frac{1}{z_{out}} \right) + (z_{in} + \delta_E) F_c - \frac{8}{15} E_{eq} \sqrt{R_{eq}} \delta_E^{2.5} \quad (27)$$

Finally, the cohesion energy with the JKR model can be expressed as a function of the pull-off force,  $F_P$ :

$$E_{coh} = \frac{1}{45} \left( 54 + 6^{\frac{2}{3}} \right) \delta_E F_P \quad (28)$$

The detailed calculation of cohesion energies is reported in Appendix B. By combining Equation (A54) with one of the expression of the cohesion energy (Equations (28), (A19) and (A37)), a fully predictive model is obtained.

#### 4.5. Comparison with DEM Simulations

In order to validate the developed analytical model (Equation (A54)), DEM simulations were carried out with the SJKR cohesion model, by considering a Bond number  $Bo = 500$ . The configuration of the simulations is the same as Figure 6: there is an API particle adhered to a carrier particle, which has a well-defined initial velocity. Nine different values of initial angle  $\theta$  were considered, ranging from 0 to  $\pi/2$ . For each angle considered, the simulations were repeated at different initial velocity values, progressively narrowing the velocity interval until the escape velocity could be determined up to two decimal points. The results can be compared with the values estimated by the analytical model and are shown in Figure 8. The plot shows an excellent agreement between the analytical predictions and the values obtained by the detailed DEM simulations.

Interestingly, the escape velocity of a particle at the south pole is two orders of magnitude smaller than the escape velocity of a particle in equatorial position. In general, as the angle  $\theta$  increases (and therefore as the particle moves from the equator to the south pole), the escape velocity value decreases.

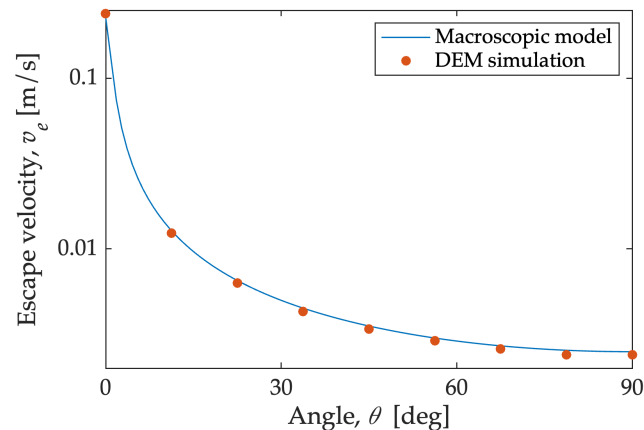


**Figure 8.** Comparison between analytical model for the escape velocity (Equation (A54)) and DEM simulations with MFIX (SJKR cohesion model).

#### 4.6. Effect of the Carrier–Wall Collision Dynamics

The analytical model correctly describes the case in which the API particle, adhering to the stationary carrier, impulsively acquires a velocity. This simplified representation of the collision does not take the transient variation of carrier velocity (slow down and then start of the rebound) along the carrier impact duration. Indeed, following the collision, the carrier particle and the API particle, previously travelling together, will have a relative velocity other than zero (see Figure 4).

It is therefore important to quantify the possible effect of the carrier collision dynamics on the predictive capability of the analytical model for the escape velocity. The developed macroscopical model can be compared to the results presented in Table 3, related to simulations with an actual impact between the carrier particle and the wall for different values of the Bond number. The cohesion model considered is SJKR, and the physical and mechanical properties of the particles involved are the ones reported in Table 1.

Figure 9 shows the curve obtained with the macroscopical model (Equation (A54)) along with the points obtained with simulations with and without rolling friction.

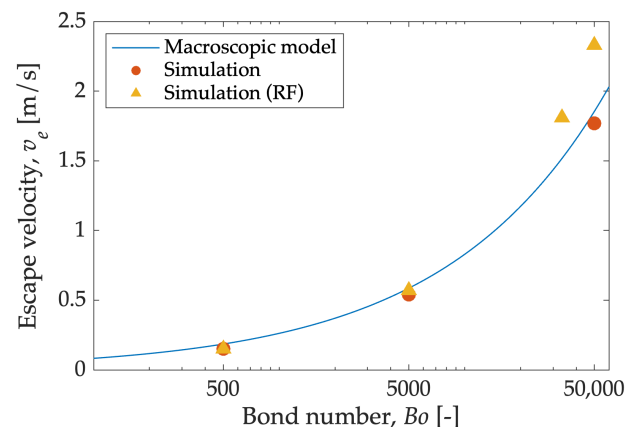


**Figure 9.** Escape velocity as a function of Bond number calculated by the macroscopic analytical model and compared to DEM simulations with and without rolling friction (RF).

It is observed that the curve correctly fits the results of the simulations, especially for values of the Bond number up to 5000, both whether rolling friction is considered or not. As the Bond number increases, the analytical model yields a reasonable estimate of the escape velocity if rolling friction is not considered; with rolling friction, a more realistic condition, the calculated escape velocity is underestimated by a maximum of 24% at  $Bo = 50,000$ .

#### 4.7. Effect of the Cohesion Model on Escape Velocity

The model obtained for the escape velocity can be applied to evaluate how the escape velocity varies as a function of the cohesion model selected in the simulations. The parameters of the cohesive models have been chosen with reference to an adhesion force value equal to 500 times the weight of the API particle ( $Bo = 500$ ), that is:  $F = 3.8$  nN. In the case of VDW, this is the cohesive/adhesive force at zero overlap ( $F_c$ ). In the case of SJKR, that value is set as the force at the equilibrium between Hertz and cohesive force. Initially the API particles are in equilibrium with the carrier. Additional information about the cohesive parameter selection with the three models is reported in Appendix C. The parameters for the cohesion models are reported in Table 4.

**Table 4.** Cohesion parameters for SJKR, JKR and VDW models by considering  $Bo = 500$ .

|                                                         |                      |
|---------------------------------------------------------|----------------------|
| SJKR cohesion energy density, $k$ (J/m <sup>3</sup> )   | 40,420               |
| JKR surface energy, $\gamma_{jkr}$ (mJ/m <sup>2</sup> ) | 0.086                |
| VDW surface energy, $\gamma_{vdw}$ (mJ/m <sup>2</sup> ) | 0.062                |
| Hamaker constant, $A$ (J)                               | $7.5 \cdot 10^{-22}$ |
| Outer cutoff, $z_{out}$ (nm)                            | 6.0                  |
| Inner cutoff, $z_{in}$ (nm)                             | 0.4                  |

Figure 10 shows the results obtained with the macroscopic model (Equation (A53)) for different angles and for the different cohesion models. Note the very wide variability of the escape velocity as a function of the angular position, which requires the log scale on the vertical axis.

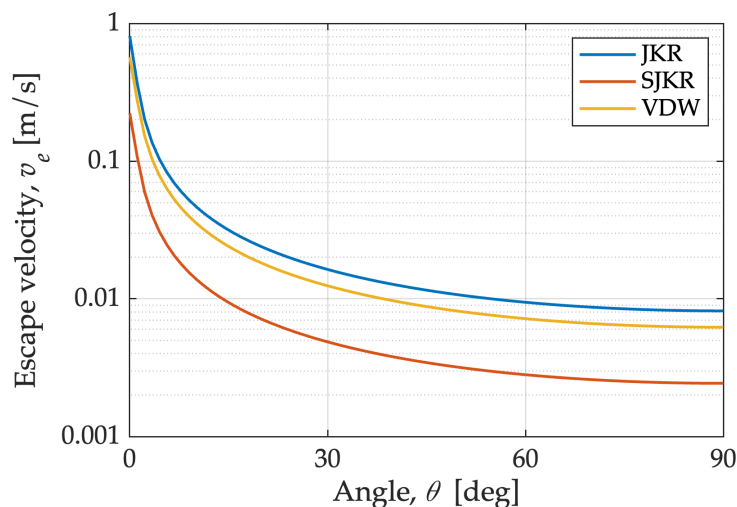


**Figure 10.** Escape velocity as a function of angle for different cohesion models.

It is observed that with the SJKR model, detachment is easier than with the other two cohesion models. This result could have been predicted by observing Figure 7, in which it is evident that the area for SJKR is smaller than that for VDW which is in turn smaller than that for JKR.

The results obtained in the analyses above suggest that the SJKR model may underestimate the impact of cohesive forces and result in an unrealistically “simple” deaggregation mechanics. The VDW model, on the other hand, with properly selected parameters, can provide results similar (within 29%) to the JKR model, for which it can represent a valid, lower computational effort alternative.

#### 4.8. Relation with Actual Deaggregation Conditions

With the escape velocity model, it is possible to evaluate whether the carrier–wall impact mechanism can actually be sufficient to promote the complete deaggregation of the

fine ingredient. Both Alfano et al. [22] and Sommerfeld and Schmalfuß [37] report typical impact velocities of about 3–4 m/s. This value can be compared with the escape velocity values calculated by the analytical model; if such value is lower than the impact velocity, the particle will likely detach. The comparison is made considering an API particle in equatorial position (therefore more difficult to detach), the JKR model, a 100  $\mu\text{m}$  carrier particle, and three different adhesion levels: low (adhesive force: 2.5 nN), medium (adhesive force: 25 nN), high (adhesive force: 250 nN). The calculated escape velocity is shown in Figure 11 as a function of the API diameter, along with a dashed line representing the typical carrier–wall impact velocity reported in literature and a corresponding “detachment area”.

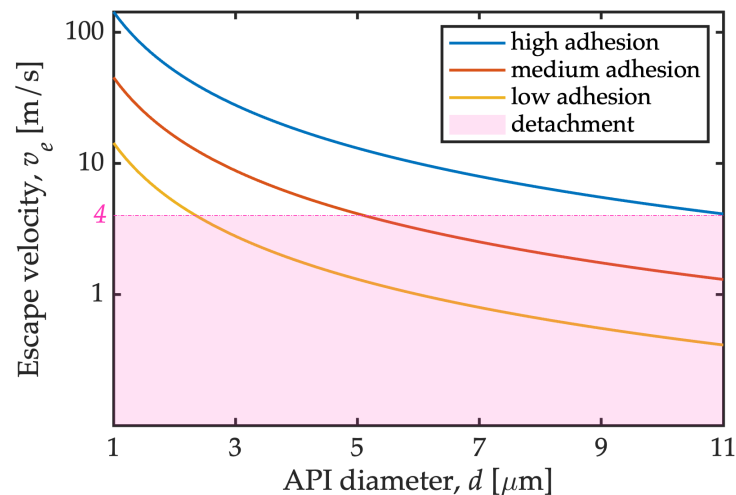


**Figure 11.** Escape velocity of particles in equatorial position as a function of API diameter and adhesion force (low: 2.5 nN, medium: 25 nN, high: 250 nN). The dashed line denotes the typical carrier–wall impact velocity reported in the literature [22,37].

It can be observed that the detachment of submicrometric particles the equatorial position would require impact velocities higher than 10 m/s even with the low adhesion force. In the case of a high adhesion, impact velocities higher than 4 m/s are required even for particles with a diameter greater than 5  $\mu\text{m}$ ; yet an adhesion force of 250 nN, a reference for the case of high adhesion, is typical of commonly used formulations such as salbutamol-lactose [4,36].

It is therefore probable that a single carrier–wall impact cannot cause the complete detachment of the API particles, but that some API remain in the equatorial position with respect to the carrier–wall point of impact. It should be kept in mind that the present model is limited to considering normal impacts. While the normal component is always present in a contact, a tangential velocity component or a rotational component may also influence the detachment process. A model extension will be sought in the near future to account for all such effects, following approaches similar to Ariane et al. [16] and Schulz et al. [20]. In order for complete carrier deaggregation, other mechanisms should be incorporated, such as subsequent impacts or fluid dynamics effects.

## 5. Conclusions

The deaggregation of API particles due to normal carrier–wall collisions has been investigated in detail with DEM simulations by considering a single API particles attached to a carrier in equatorial position. The collision dynamics and the escape velocity, i.e., the critical impact velocity of the carrier above which API deaggregation occurs, has been evaluated as a function of the granular Bond number. The escape velocity values vary between 0.15 and 1.77 m/s depending on the Bond number considered, 500 and 50,000, respectively. If rolling friction is (more realistically) considered, the escape velocity turns out to be higher than without rolling friction.

An increase in the escape velocity is observed with higher values of the static friction or lower values of the restitution coefficient, highlighting the importance of correctly evaluating these mechanical properties of the powders. The effect of rolling friction on the contact dynamics was further analyzed, evaluating in detail the velocity, angular velocity and overlap profiles of both the API and the carrier during carrier–wall impact. If rolling friction is not activated, the API particle (if not detached) orbits indefinitely on the carrier with a high angular velocity and with an overlap lower than the initial one. The addition of rolling friction dampens this rolling motion, limiting the increase in angular velocity and stabilizing the fine particle.

A more general, elegant analytical model to estimate the escape velocity is derived and presented, which allows estimating in a simple and effective way the critical detachment velocity of the API from the carrier as a function of the particle properties and a generic API particle position on the carrier surface. After a comparison with sets of DEM simulations which corroborated the validity of the analytical model calculations, the dependence of the critical velocity on the choice of the cohesion model, under comparable conditions, has been discussed in detail.

Finally, the analytically predicted escape velocity has been compared to typical carrier–wall impact velocities reported in literature, deriving interesting conclusions on the role of the API particle size and the fraction of fine API potentially deaggregating.

Overall, the present study contributes to a greater understanding and prediction of the phenomenon of detachment of the active ingredient due to particle–wall collisions by examining the role of contact model and parameters and through the development of an analytical model for the escape velocity, which may be extremely useful whenever typical normal impact velocities in inhalers can be estimated. The obtained results highlighted the importance of the choice of models and parameters in DEM simulations, such as cohesion and friction, whose selection is often overlooked in modelling studies. Furthermore, the simple and effective macroscopic model allows a quick estimate of the escape velocity as a function of the physical and mechanical parameters of the materials involved.

**Author Contributions:** Conceptualization, A.B., R.G. and F.O.A.; methodology, A.D.R.; software, F.P.D.M. and A.D.R.; validation, F.O.A. and F.P.D.M.; formal analysis, F.O.A., A.D.R. and F.P.D.M.; investigation, F.O.A., A.D.R. and F.P.D.M.; data curation, F.O.A.; writing—original draft preparation, F.O.A.; writing—review and editing, A.D.R. and F.P.D.M.; visualization, F.O.A.; supervision, R.G. and A.D.R. All authors have read and agreed to the published version of the manuscript.

**Funding:** This research received no external funding.

**Institutional Review Board Statement:** Not applicable.

**Informed Consent Statement:** Not applicable.

**Data Availability Statement:** The data presented in this study not already contained in the article and appendices are available on request from the corresponding authors.

**Conflicts of Interest:** The authors declare no conflict of interest.

## Abbreviations

The following abbreviations are used in this manuscript:

|      |                                                    |
|------|----------------------------------------------------|
| API  | Active Pharmaceutical Ingredient                   |
| DPI  | Dry Powder Inhaler                                 |
| JKR  | Johnson–Kendall–Roberts contact model              |
| SJKR | Linear cohesion model                              |
| VDW  | Constant cohesion model                            |
| CDT  | Constant Directional Torque rolling friction model |
| AFM  | Atomic force microscopy                            |
| RF   | Rolling friction                                   |
| PP   | Particle–particle                                  |
| PW   | Particle–wall                                      |

## Nomenclature

The following symbols are used in this manuscript:

|                  |                                           |
|------------------|-------------------------------------------|
| $\vec{x}_i$      | Position vector of particle $i$           |
| $\vec{v}_i$      | Velocity vector of particle $i$           |
| $\vec{\omega}_i$ | Angular velocity vector of particle $i$   |
| $N_C$            | Number of particles $i$                   |
| $\vec{F}_T$      | Total force                               |
| $\vec{F}_c$      | Contact force                             |
| $\vec{F}_{c,oh}$ | Cohesion force                            |
| $\vec{F}_d$      | Drag force                                |
| $\vec{F}_p$      | Pressure gradient force                   |
| $\vec{F}_l$      | Lift force                                |
| $\vec{F}_g$      | Gravity force                             |
| $\vec{T}_T$      | Total torque                              |
| $\vec{T}_c$      | Contact torque                            |
| $\vec{T}_r$      | Rolling resistance torque                 |
| $E_{eq}$         | Equivalent Young modulus                  |
| $G_{eq}$         | Equivalent shear modulus                  |
| $R_{eq}$         | Equivalent radius                         |
| $\delta_n$       | Normal overlap                            |
| $\delta_t$       | Tangential overlap                        |
| $v_n$            | Normal impact velocity                    |
| $v_t$            | Tangential impact velocity                |
| $\eta_n^H$       | Normal damping coefficient                |
| $\eta_t^H$       | Tangential damping coefficient            |
| $\mu_s$          | Static friction coefficient               |
| $\mu_r$          | Rolling friction coefficient              |
| $a$              | Radius of the contact area                |
| $A_{cont}$       | Contact area                              |
| $\gamma$         | Cohesion surface energy (JKR, VDW models) |
| $k$              | Cohesion energy density (SJKR model)      |
| $z_{in}$         | Inner cutoff for cohesive forces          |
| $z_{out}$        | Outer cutoff for cohesive forces          |
| $m$              | Particle mass                             |
| $R$              | Particle radius                           |
| $\rho$           | Density                                   |
| $E$              | Young modulus                             |
| $\nu$            | Poisson coefficient                       |
| $e$              | Coefficient of restitution                |
| $Bo$             | Bond number                               |
| $F_E$            | Equilibrium force                         |
| $\delta_E$       | Equilibrium overlap (normal)              |
| $v_e$            | Escape velocity                           |
| $E_k$            | Kinetic energy                            |
| $E_{coh}$        | Cohesion energy                           |
| $F_{fc}$         | Centrifugal force                         |
| $L_{fc}$         | Work of the centrifugal force             |
| $\theta$         | API angular position on carrier           |

## Appendix A. Conversion of Translational Energy

Consider a spherical particle moving on a wall with an initial velocity,  $v_0$  (Figure A1, left). The particle initially has a zero angular velocity ( $\omega_0 = 0$ ).

A constant static friction force,  $F_A$ , acts between the wall and the particle and is equal to:

$$F_A = \mu_s mg \quad (A1)$$

where  $\mu_s$  is the static friction coefficient,  $m$  is the mass of the particle,  $g$  is the gravitational acceleration.



**Figure A1.** Particle sliding on a wall with initial velocity  $v_0$ . Due to attrition, the translational energy is progressively converted into rotational energy.

The particle, initially sliding on the wall, begins to acquire an angular velocity,  $\omega$ , due to the presence of the frictional force (Figure A1, right). The translational energy of the particle is progressively converted into rotational energy. The translational velocity,  $v(t)$ , the angular velocity and the position of the particle,  $x(t)$ , are given by force and torque balances:

$$v(t) = v_0 - \frac{F_A}{m}t = v_0 - \mu_s g \cdot t \quad (\text{A2})$$

$$\omega(t) = \frac{F_A R}{I}t = \frac{5\mu_s g}{2R}t \quad (\text{A3})$$

$$x(t) = v_0 t - \frac{1}{2}\mu_s g t^2 \quad (\text{A4})$$

where  $I = \frac{2}{5}mR^2$  is the moment of inertia of the spherical particle.

At a certain instant,  $t_{PR}$ , a pure rolling motion will begin, during which the particle will no longer slide on the wall. The relationship between angular velocity and translational velocity at instant  $t_{PR}$  is as follows:

$$\omega(t_{PR}) = \frac{v(t_{PR})}{R} \quad (\text{A5})$$

By substituting in Equations (A2) and (A3):

$$\frac{5}{2} \frac{\mu_s g}{R} t_{PR} = \frac{v_0 - \mu_s g t_{PR}}{R} \quad (\text{A6})$$

from which  $t_{PR}$  can be calculated:

$$t_{PR} = \frac{2}{7} \frac{v_0}{\mu_s g} \quad (\text{A7})$$

The distance traveled before pure rolling begins can be calculated by substituting this value in Equation (A4):

$$L = x(t_{PR}) = \frac{2}{7} \frac{v_0^2}{\mu_s g} - \frac{1}{2} \mu_s g t_{PR}^2 = \frac{12}{49} \frac{v_0^2}{\mu_s g} \quad (\text{A8})$$

The sliding motion induces a dissipation which, once the distance traveled  $L$  is known, can be calculated as:

$$W_T = F_A \cdot L = \mu_s g t_{PR} \cdot \frac{12}{49} \frac{v_0^2}{\mu_s g} = \frac{12}{49} m v_0^2 \quad (\text{A9})$$

The rolling motion also induces dissipation. The angle traveled before pure rolling begins is given by:

$$\theta = \int_0^{t_{PR}} \omega(t) dt = \frac{5}{49} \frac{1}{\mu_s g} \cdot \frac{v_0^2}{R} \quad (\text{A10})$$

The dissipation due to rolling until time  $t_{PR}$  is given by:

$$W_R = F_A \cdot R \cdot \theta = \mu_s mgR \cdot \frac{5}{49} \frac{1}{\mu_s g} \cdot \frac{v_0^2}{R} = \frac{5}{49} mv_0^2 \quad (\text{A11})$$

The initial kinetic energy of the particle is:

$$E_0 = \frac{1}{2} mv_0^2 \quad (\text{A12})$$

while its kinetic energy at time  $t_{PR}$  is:

$$E_f = \frac{1}{2} mv_f^2 + \frac{1}{2} I\omega_f^2 = \frac{1}{2} mv_f^2 + \frac{1}{2} \cdot \frac{2}{5} mR^2 \cdot \frac{v_f^2}{R^2} = \frac{7}{10} mv_f^2 \quad (\text{A13})$$

From the conservation of energy:

$$E_f = E_0 - W_T + W_R \quad (\text{A14})$$

$$\frac{7}{10} mv_f^2 = \frac{1}{2} mv_0^2 - \frac{12}{49} mv_0^2 + \frac{5}{49} mv_0^2 \quad (\text{A15})$$

$$E_f = E_0 - W_T + W_R \quad (\text{A16})$$

$$v_f^2 = \frac{10}{7} \left( \frac{1}{2} - \frac{12}{49} + \frac{5}{49} \right) v_0^2 = \frac{10}{7} \cdot \frac{5}{14} v_0^2 = \frac{25}{49} v_0^2 \quad (\text{A17})$$

The velocity of the particle at time  $t_{PR}$  can finally be expressed as a function of initial velocity,  $v_0$ :

$$v_f = \frac{5}{7} v_0 \quad (\text{A18})$$

It is interesting to note that  $v_f$  does not depend on the static friction coefficient, although it affects the time  $t_{PR}$ .

In Figure 5c it was observed that the final velocity of the API particle (no RF) rolling on the carrier's surface was equal to 10/7 of the initial one. Considering that the carrier velocity variation is  $2v_0$  (the carrier goes from  $-1$  m/s to  $+1$  m/s), the final velocity of the API particle is in line with the analytical considerations just presented.

## Appendix B. Cohesion Energy

### Appendix B.1. SJKR Model

The SJKR model does not provide for long-range cohesive contributions, so the detachment occurs if the overlap becomes zero. By referring to the formulation of the contact area according to the Hertz theory (see Equation (10)),  $E_{coh}$  can be calculated as:

$$E_{coh} = \int_0^{\delta_E} F_{sjkr} d\delta = \frac{k\pi R_{eq}}{2} \delta_E^2 - \frac{8}{15} E_{eq} \sqrt{R_{eq}} \delta_E^{2.5} \quad (\text{A19})$$

### Appendix B.2. JKR Model

The JKR model can be expressed in a dimensionless form by expressing the variables as a function of the equilibrium overlap and pull-off force. The pull-off force  $F_P$ , the value of the force beyond which the detachment takes place, is given by:

$$F_P = -3\pi\gamma R_{eq} \quad (\text{A20})$$

The equilibrium overlap is the displacement at which the force is zero ( $F_{el,JKR} = 0$ ), so there is an equilibrium between the cohesive contribution and the elastic contribution.

The value of the radius of the contact area ( $a_E$ ) and of the overlap ( $\delta_E$ ) at this point are given by:

$$a_E = \left( 9\pi\gamma \frac{R_{eq}^2}{E_{eq}} \right)^{\frac{1}{3}} \tag{A21}$$

$$\delta_E = \left( \frac{\pi\gamma\sqrt{3R_{eq}}}{E_{eq}} \right)^{\frac{2}{3}} \tag{A22}$$

If  $a^* = a/a_E$ ,  $\delta^* = \delta/\delta_E$ , and  $F^* = F/F_P$ , the functional relationships of the JKR model can be expressed by:

$$\delta^* = \left( 3a^{*2} - 2\sqrt{a^*} \right) \tag{A23}$$

$$F^* = 4 \left( -a^{*3} + a^{*1.5} \right) \tag{A24}$$

The dimensionless force–displacement graph for the JKR model is shown in Figure A2, along with the coordinates of the points of interest.

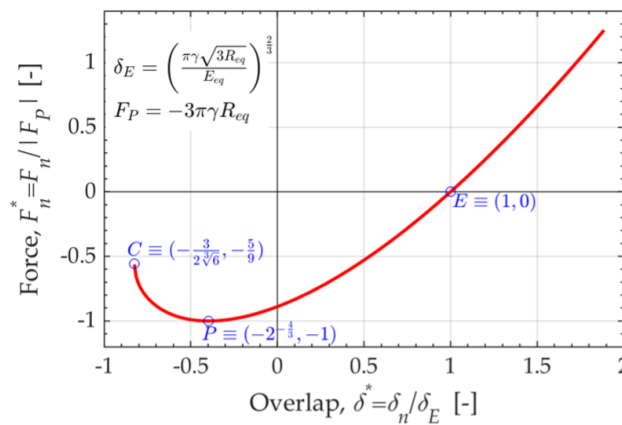


**Figure A2.** Force–displacement relationship with JKR model in dimensionless variables.

With the JKR model detachment occurs at a negative overlap, so the cohesion energy is the definite integral of the force from  $\delta_C$  to  $\delta_E$  (see Figure A2):

$$E_{coh} = \int_{\delta_C}^{\delta_E} F_{jkr} d\delta \tag{A25}$$

The overlap is given by:

$$\delta = \delta_E \left( 3a^{*2} - 2\sqrt{a^*} \right) \tag{A26}$$

From Equation (A26), one can calculate:

$$d\delta = \delta_E \cdot 6a^* da^* - 2\delta_E \cdot \frac{1}{2\sqrt{a^*}} da^* \tag{A27}$$

Substituting in Equation (A25), the integral can be expressed as:

$$E_{coh} = \int_{a^*(C)}^{a^*(E)} 4F_P \left( -a^{*3} + a^{*1.5} \right) \left( \delta_E \cdot 6a^* da^* - 2\delta_E \cdot \frac{1}{2\sqrt{a^*}} da^* \right) \tag{A28}$$

Hence, with simple algebraic passages:

$$E_{coh} = -8F_P\delta_E \int_{a^*(c)}^{a^*(E)} \left( -a^{*3} + a^{*1.5} \right) \cdot \frac{1}{2\sqrt{a^*}} da^* \tag{A29}$$

The limits of integration need to be made explicit. Point E is the point at which  $F_{jkr} = 0$ :

$$a^*(E) = 1 \quad (\text{A30})$$

Point C corresponds to the point at which  $\frac{d\delta}{dF_{jkr}} = 0$ :

$$a^*(C) = 6^{-\frac{2}{3}} \quad (\text{A31})$$

The definite integral in Equation (A29) can now be solved, giving:

$$E_{coh} = \frac{1}{45} \left( 54 + 6^{\frac{2}{3}} \right) \delta_E F_P \quad (\text{A32})$$

### Appendix B.3. VDW Model

As shown in Figure A3, three distinct sections can be identified in the model curve of the VDW cohesion model.

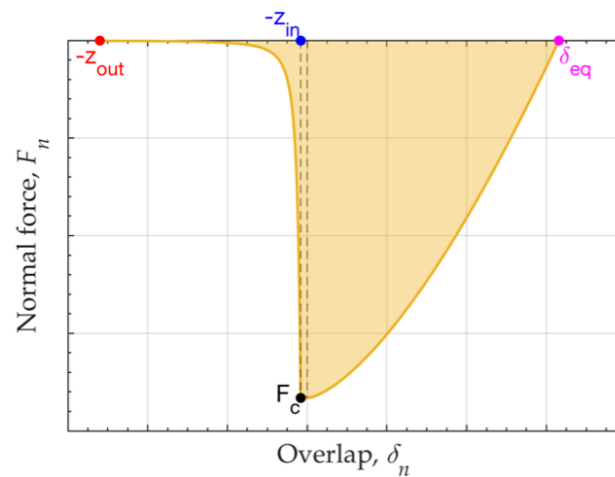


**Figure A3.** Normal force vs. overlap according to the VDW cohesion model.

The cohesion energy can be thus expressed as the sum of three contributions:

$$E_{coh} = E_{coh,1} + E_{coh,2} + E_{coh,3} \quad (\text{A33})$$

with:

$$E_{coh,1} = \int_{-z_{out}}^{-z_{in}} \frac{AR_{eq}}{6\delta^2} d\delta = \frac{AR_{eq}}{6} \left( \frac{1}{z_{in}} - \frac{1}{z_{out}} \right) \quad (\text{A34})$$

$$E_{coh,2} = \int_{-z_{in}}^0 F_C d\delta = z_{in} \cdot F_C \quad (\text{A35})$$

$$E_{coh,3} = \int_0^{\delta_E} F_C d\delta - \int_0^{\delta_E} F_{Hertz} d\delta = F_C \delta_E - \frac{8}{15} E_{eq} \sqrt{R_{eq}} \delta_E^{2.5} \quad (\text{A36})$$

By adding the three terms of Equations (A34)–(A36), the following expression of the cohesion energy is obtained:

$$E_{coh} = A \frac{R_{eq}}{6} \left( \frac{1}{z_{in}} - \frac{1}{z_{out}} \right) + (z_{in} + \delta_E) F_C - \frac{8}{15} E_{eq} \sqrt{R_{eq}} \delta_E^{2.5} \quad (\text{A37})$$

## Appendix C. Additional Relationships for the Escape Velocity

### Appendix C.1. Derivation of Cohesion Model Parameters

The material parameter for cohesion must be derived consistently across the different models. We consider a reference value for the cohesive force, from which we calculate

the cohesion parameters for the different models. Having set the Bond number,  $Bo = \frac{F_c}{F_g}$ , we obtain:

$$F_{eq} = Bo \cdot m_{API} g \quad (A38)$$

#### Appendix C.1.1. SJKR Model

From the assumption of equilibrium between the cohesive and elastic forces, the equilibrium displacement is:

$$\delta_{eq} = R_{eq} \left( \frac{3}{4} \pi \frac{k_{coh}}{E_{eq}} \right)^2 \quad (A39)$$

The Hertzian force at this equilibrium displacement is

$$F_H(\delta_{eq}) = \frac{4}{3} E_{eq} \sqrt{R_{eq} \delta_{eq}^3} = \frac{9}{16} R_{eq}^2 \frac{\pi^3}{E_{eq}^2} k_{coh}^3 \quad (A40)$$

and by expressing the equilibrium force as a function of  $Bo$ , one obtains

$$k_{coh} = \frac{4}{3\pi} \sqrt[3]{Bo \cdot m_{API} g \frac{E_{eq}^2}{R_{eq}^2}} \quad (A41)$$

#### Appendix C.1.2. JKR Model

Assuming that the reference value for the cohesive force is equal to the pull-off force of the JKR model, we calculate:

$$\gamma_{JKR} = \frac{F_{eq}}{3\pi R_{eq}} = \frac{Bo \cdot m_{API} g}{3\pi R_{eq}} \quad (A42)$$

The equilibrium overlap is given by:

$$\delta_{eq} = \left( \pi \sqrt{3R_{eq}} \frac{\gamma_{JKR}}{E_{eq}} \right)^{\frac{2}{3}} \quad (A43)$$

With the corresponding equilibrium force expressed by:

$$F_H(\delta_{eq}) = \frac{4}{3} E_{eq} \sqrt{R_{eq} \delta_{eq}^3} = \frac{4}{\sqrt{3}} \pi R_{eq} \gamma_{JKR} \quad (A44)$$

#### Appendix C.1.3. VDW Model

The cohesive force is summed to the elastic force. So, deriving  $\delta_{eq}$  from the assumption of the equilibrium between the cohesive and elastic forces:

$$\delta_{eq} = \left( 3\pi \sqrt{R_{eq}} \frac{\gamma_{VDW}}{E_{eq}} \right)^{\frac{2}{3}} \quad (A45)$$

$$F_H(\delta_{eq}) = \frac{4}{3} E_{eq} \sqrt{R_{eq} \delta_{eq}^3} = 4\pi R_{eq} \gamma_{VDW} \quad (A46)$$

$$\gamma_{VDW} = \frac{3}{4} \gamma_{JKR} \quad (A47)$$

#### Appendix C.2. Equatorial Velocity ( $0^\circ$ )

$$\frac{m_{API}}{R_C + R_{API}} v_0^2 \delta_{eq} = E_{coh} \quad (A48)$$

$$v_0 = \sqrt{\frac{E_{coh}}{m_{API} \frac{\delta_{eq}}{R_C + R_{API}}}} \quad (\text{A49})$$

### Appendix C.3. South Pole Velocity (90°)

$$\frac{1}{2} m_{API} v_{90}^2 = E_{coh} \quad (\text{A50})$$

$$v_{90} = \sqrt{\frac{E_{coh}}{\frac{1}{2} m_{API}}} \quad (\text{A51})$$

### Appendix C.4. Velocity Ratio

$$\frac{v_0}{v_{90}} = \sqrt{\frac{R_C + R_{API}}{2\delta_{eq}}} \quad (\text{A52})$$

### Appendix C.5. General South-Hemisphere Detachment

By making use of the previous results ( $v_0$ , Equation (A49) and  $v_{90}$ , Equation (A51)), the escape velocity can be expressed as:

$$v_e = \sqrt{\frac{1}{\frac{1}{v_0^2} \cos^2 \theta + \frac{1}{v_{90}^2} \sin^2 \theta}} \quad (\text{A53})$$

More explicitly,

$$v_e = \sqrt{\frac{E_{coh}/m_{API}}{\frac{\delta_0}{R_C + R_{API}} \cos^2 \theta + \frac{1}{2} \sin^2 \theta}} \quad (\text{A54})$$

### Appendix C.6. Alternative Relationships

From

$$\left(\frac{v}{v_0}\right)^2 \cos^2 \theta + \left(\frac{v}{v_{90}}\right)^2 \sin^2 \theta = 1 \quad (\text{A55})$$

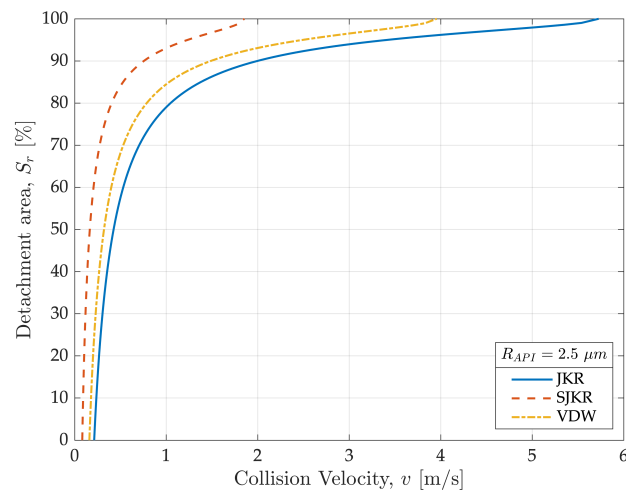
$$\sin \theta = \sqrt{\frac{1 - \left(\frac{v}{v_0}\right)^2}{\left(\frac{v}{v_{90}}\right)^2 - \left(\frac{v}{v_0}\right)^2}} = \sqrt{\frac{\left(\frac{v_0}{v}\right)^2 - 1}{\left(\frac{v_0}{v_{90}}\right)^2 - 1}} \approx \frac{v_{90}}{v_0} \sqrt{\left(\frac{v_0}{v}\right)^2 - 1} \quad (\text{A56})$$

$$\theta = \arcsin \sqrt{\frac{\left(\frac{v_0}{v}\right)^2 - 1}{\left(\frac{v_0}{v_{90}}\right)^2 - 1}} \quad (\text{A57})$$

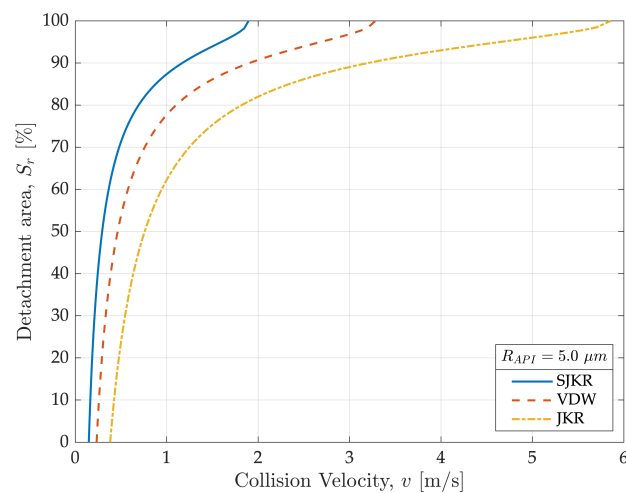
The uncovered surface fraction of the hemisphere  $S_r$  is:

$$S_r = 1 - \sin \theta = 1 - \sqrt{\frac{\left(\frac{v_0}{v}\right)^2 - 1}{\left(\frac{v_0}{v_{90}}\right)^2 - 1}} \quad (\text{A58})$$

The fraction of uncovered surface as a function of collision velocity is shown in Figure A4 for two different sizes of the API particle.



(a)



(b)

**Figure A4.** Fraction of uncovered surface vs. collision velocity.  $R_{API} = 2.5 \mu\text{m}$  (a) or  $5.0 \mu\text{m}$  (b);  $R_C = 50 \mu\text{m}$ ;  $Bo = 50,000$ .

## References

- Hoppentocht, M.; Hagedoorn, P.; Frijlink, H.; De Boer, A. Technological and practical challenges of Dry Powder Inhalers and formulations. *Adv. Drug Deliv. Rev.* **2014**, *75*, 18–31. [[CrossRef](#)] [[PubMed](#)]
- Rashid, M.A.; Muneer, S.; Mendhi, J.; Sabuj, M.Z.R.; Alhamhoom, Y.; Xiao, Y.; Wang, T.; Izake, E.L.; Islam, N. Inhaled Edoxaban dry powder inhaler formulations: Development, characterization and their effects on the coagulopathy associated with COVID-19 infection. *Int. J. Pharm.* **2021**, *608*, 121122. [[CrossRef](#)] [[PubMed](#)]
- Sommerfeld, M.; Cui, Y.; Schmalfuß, S. Potential and constraints for the application of CFD combined with Lagrangian particle tracking to Dry Powder Inhalers. *Eur. J. Pharm. Sci.* **2019**, *128*, 299–324. [[CrossRef](#)]
- Begat, P.; Morton, D.A.; Staniforth, J.N.; Price, R. The cohesive-adhesive balances in dry powder inhaler formulations I: Direct quantification by atomic force microscopy. *Pharm. Res.* **2004**, *21*, 1591–1597. [[CrossRef](#)] [[PubMed](#)]
- Zafar, U.; Alfano, F.; Ghadiri, M. Evaluation of a new dispersion technique for assessing triboelectric charging of powders. *Int. J. Pharm.* **2018**, *543*, 151–159. [[CrossRef](#)]
- Alfano, F.O.; Di Renzo, A.; Di Maio, F.P.; Ghadiri, M. Computational analysis of triboelectrification due to aerodynamic powder dispersion. *Powder Technol.* **2021**, *382*, 491–504. [[CrossRef](#)]
- Finlay, W.H. *The Mechanics of Inhaled Pharmaceutical Aerosols: An Introduction*; Academic Press: London, UK, 2001.
- Cavalli, G.; Bosi, R.; Ghiretti, A.; Cottini, C.; Benassi, A.; Gaspari, R. A shear cell study on oral and inhalation grade lactose powders. *Powder Technol.* **2020**, *372*, 117–127. [[CrossRef](#)]
- de Boer, A.H.; Hagedoorn, P.; Hoppentocht, M.; Buttini, F.; Grasmeyer, F.; Frijlink, H.W. Dry powder inhalation: Past, present and future. *Expert Opin. Drug Deliv.* **2017**, *14*, 499–512. [[CrossRef](#)]

10. Dos Reis, L.G.; Chaugule, V.; Fletcher, D.F.; Young, P.M.; Traini, D.; Soria, J. In-vitro and particle image velocimetry studies of dry powder inhalers. *Int. J. Pharm.* **2021**, *592*, 119966. [[CrossRef](#)]
11. Pasquali, I.; Merusi, C.; Brambilla, G.; Long, E.J.; Hargrave, G.K.; Versteeg, H.K. Optical diagnostics study of air flow and powder fluidisation in Nexthaler<sup>®</sup>—Part I: Studies with lactose placebo formulation. *Int. J. Pharm.* **2015**, *496*, 780–791. [[CrossRef](#)]
12. Fletcher, D.F.; Chaugule, V.; Gomes dos Reis, L.; Young, P.M.; Traini, D.; Soria, J. On the use of computational fluid dynamics (CFD) modelling to design improved dry powder inhalers. *Pharm. Res.* **2021**, *38*, 277–288. [[CrossRef](#)] [[PubMed](#)]
13. Merusi, C.; Brambilla, G.; Long, E.; Hargrave, G.; Versteeg, H. Optical diagnostics studies of air flow and powder fluidisation in Nexthaler<sup>®</sup>. Part II: Use of fluorescent imaging to characterise transient release of fines from a dry powder inhaler. *Int. J. Pharm.* **2018**, *549*, 96–108. [[CrossRef](#)] [[PubMed](#)]
14. Kou, X.; Wereley, S.T.; Heng, P.W.; Chan, L.W.; Carvajal, M.T. Powder dispersion mechanisms within a dry powder inhaler using microscale particle image velocimetry. *Int. J. Pharm.* **2016**, *514*, 445–455. [[CrossRef](#)] [[PubMed](#)]
15. Benassi, A.; Cottini, C. Numerical Simulations for Inhalation Product Development: Achievements and Current Limitations. *ONdrugDelivery* **2021**, *127*, 68–75.
16. Ariane, M.; Sommerfeld, M.; Alexiadis, A. Wall collision and drug-carrier detachment in dry powder inhalers: Using DEM to devise a sub-scale model for CFD calculations. *Powder Technol.* **2018**, *334*, 65–75. [[CrossRef](#)]
17. Sarangi, S.; Thalberg, K.; Frenning, G. Effect of carrier size and mechanical properties on adhesive unit stability for inhalation: A numerical study. *Powder Technol.* **2021**, *390*, 230–239. [[CrossRef](#)]
18. Tamadondar, M.R.; Rasmuson, A. The effect of carrier surface roughness on wall collision-induced detachment of micronized pharmaceutical particles. *AIChE J.* **2020**, *66*, e16771. [[CrossRef](#)]
19. Tong, Z.; Kamiya, H.; Yu, A.; Chan, H.K.; Yang, R. Multi-scale modelling of powder dispersion in a carrier-based inhalation system. *Pharm. Res.* **2015**, *32*, 2086–2096. [[CrossRef](#)]
20. Schulz, D.; Woschny, N.; Schmidt, E.; Kruggel-Emden, H. Modelling of the detachment of adhesive dust particles during bulk solid particle impact to enhance dust detachment functions. *Powder Technol.* **2022**, *400*, 117238. [[CrossRef](#)]
21. Yang, J.; Wu, C.Y.; Adams, M. Three-dimensional DEM–CFD analysis of air-flow-induced detachment of API particles from carrier particles in dry powder inhalers. *Acta Pharm. Sin. B* **2014**, *4*, 52–59. [[CrossRef](#)]
22. Alfano, F.O.; Benassi, A.; Gaspari, R.; Di Renzo, A.; Di Maio, F.P. Full-Scale DEM Simulation of Coupled Fluid and Dry-Coated Particle Flow in Swirl-Based Dry Powder Inhalers. *Ind. Eng. Chem. Res.* **2021**, *60*, 15310–15326. [[CrossRef](#)]
23. Zhao, J.; Haghnegahdar, A.; Feng, Y.; Patil, A.; Kulkarni, N.; Singh, G.J.P.; Malhotra, G.; Bharadwaj, R. Prediction of the carrier shape effect on particle transport, interaction and deposition in two dry powder inhalers and a mouth-to-G13 human respiratory system: A CFD-DEM study. *J. Aerosol Sci.* **2022**, *160*, 105899. [[CrossRef](#)]
24. Tong, Z.; Yang, R.; Yu, A. CFD-DEM study of the aerosolisation mechanism of carrier-based formulations with high drug loadings. *Powder Technol.* **2017**, *314*, 620–626. [[CrossRef](#)]
25. Alfano, F.; Di Maio, F.; Di Renzo, A. Deagglomeration of selected high-load API-carrier particles in swirl-based dry powder inhalers. *Powder Technol.* **2022**, *408*, 117800. [[CrossRef](#)]
26. Garg, R.; Galvin, J.; Li, T.; Pannala, S. Open-source MFIX-DEM software for gas-solids flows: Part I-Verification studies *Powder Technol.* **2012**, *220*, 122–137. [[CrossRef](#)]
27. Tsuji, Y.; Kawaguchi, T.; Tanaka, T. Discrete particle simulation of two-dimensional fluidized bed. *Powder Technol.* **1993**, *77*, 79–87. [[CrossRef](#)]
28. Di Renzo, A.; Di Maio, F. Comparison of contact-force models for the simulation of collisions in DEM-based granular flow codes. *Chem. Eng. Sci.* **2004**, *59*, 525–541. [[CrossRef](#)]
29. Ai, J.; Chen, J.F.; Rotter, J.; Ooi, J. Assessment of rolling resistance models in discrete element simulations. *Powder Technol.* **2011**, *206*, 269–282. [[CrossRef](#)]
30. Johnson, K.L.; Kendall, K.; Roberts, A.D. Surface energy and the contact of elastic solids. *Proc. R. Soc. Lond. A Math. Phys. Sci.* **1971**, *324*, 301–313. [[CrossRef](#)]
31. Kloss, C.; Goniva, C.; Hager, A.; Amberger, S.; Pirker, S. Models, algorithms and validation for opensource DEM and CFD–DEM. *Prog. Comput. Fluid Dyn. Int. J.* **2012**, *12*, 140–152. [[CrossRef](#)]
32. DEM Solutions Ltd. *EDEM 2.6 User Guide*; Technical Report; Altair Engineering, Inc.: Edinburgh, UK, 2014.
33. Galvin, J.E.; Benyahia, S. The effect of cohesive forces on the fluidization of aeratable powders. *AIChE J.* **2014**, *60*, 473–484. [[CrossRef](#)]
34. Castellanos, A. The relationship between attractive interparticle forces and bulk behaviour in dry and uncharged fine powders. *Adv. Phys.* **2005**, *54*, 263–376. [[CrossRef](#)]
35. Siliveru, K.; Jange, C.; Kwek, J.; Ambrose, R. Granular bond number model to predict the flow of fine flour powders using particle properties. *J. Food Eng.* **2017**, *208*, 11–18. [[CrossRef](#)]
36. Cui, Y.; Schmalfuß, S.; Zellnitz, S.; Sommerfeld, M.; Urbanetz, N. Towards the optimisation and adaptation of dry powder inhalers. *Int. J. Pharm.* **2014**, *470*, 120–132. [[CrossRef](#)]
37. Sommerfeld, M.; Schmalfuß, S. Numerical analysis of carrier particle motion in a dry powder inhaler. *J. Fluids Eng.* **2016**, *138*, 041308. [[CrossRef](#)]